Trace Element Compositions and Defect Structures of High-Purity Quartz from the Southern Ural Region, Russia

Jens Götze [1],*, Yuanming Pan [2], Axel Müller [3,4], Elena L. Kotova [5] and Daniele Cerin [2]

[1] Institute of Mineralogy, TU Bergakademie Freiberg, Brennhausgasse 14, 09596 Freiberg, Germany
[2] Department of Geological Sciences, University of Saskatchewan, Saskatoon, SK S7N5E2, Canada; yuanming.pan@usask.ca (Y.P.); dac176@mail.usask.ca (D.C.)
[3] Naturhistorisk Museum, Universitet i Oslo, P.O. Box 1172, Blindern, 0318 Oslo, Norway; a.b.muller@nhm.uio.no
[4] Natural History Museum, Cromwell Road, London SW7 5BD, UK
[5] Mining State University St. Petersburg, 21st Line, St. Petersburg 199106, Russia; museum_spmi@spmi.ru
* Correspondence: jens.goetze@mineral.tu-freiberg.de; Tel.: +49-3731-392638

Abstract: Quartz samples of different origin from 10 localities in the Southern Ural region, Russia have been investigated to characterize their trace element compositions and defect structures. The analytical combination of cathodoluminescence (CL) microscopy and spectroscopy, electron paramagnetic resonance (EPR) spectroscopy, and trace-element analysis by inductively coupled plasma mass spectrometry (ICP-MS) revealed that almost all investigated quartz samples showed very low concentrations of trace elements (cumulative concentrations of <50 ppm with <30 ppm Al and <10 ppm Ti) and low abundances of paramagnetic defects, defining them economically as "high-purity" quartz (HPQ) suitable for high-tech applications. EPR and CL data confirmed the low abundances of substitutional Ti and Fe, and showed Al to be the only significant trace element structurally bound in the investigated quartz samples. CL microscopy revealed a heterogeneous distribution of luminescence centres (i.e., luminescence active trace elements such as Al) as well as features of deformation and recrystallization. It is suggested that healing of defects due to deformation-related recrystallization and reorganization processes of the quartz lattice during retrograde metamorphism resulted in low concentrations of CL activator and other trace elements or vacancies, and thus are the main driving processes for the formation of HPQ deposits in the investigated area.

Keywords: quartz; cathodoluminescence; electron paramagnetic resonance; trace elements

1. Introduction

Quartz and other silica minerals are some of the most important rock-forming minerals of the Earth's crust, and are important industrial raw materials. Owing to their abundance and physical and chemical properties, natural silica raw materials have a wide range of industrial and technological applications [1,2].

In particular, high-purity quartz (HPQ), with less than 50 ppm of contaminating trace elements [3,4], is of high economic value, resulting in prices up to 20 times higher than those of low-quality ("common") silica raw materials [5,6]. High-purity quartz is of strategic importance for the high-tech industry, because it is a critical material for the manufacture of crucibles used for single crystal growth of silicon metal (needed for solar panel and micro-chip production), high-temperature lamp tubing, telecommunications, optics, and semiconductor materials. Because

of the increasing demand for HPQ there are increasing exploration activities underway to search for potential deposits worldwide.

The specific quality requirements of the quartz material are challenging with respect to analytics due to the very low concentrations (from 0.1 to 50 ppm) of impurity trace elements [2]. Natural silica materials, in particular quartz, are characterized by specific properties—including lattice defects, abundance of lattice-"foreign" trace elements, degree of recrystallization, etc.—which are the result of the regional geological history and the related specific conditions of formation. Therefore, the knowledge of the interrelations between genetic conditions and quartz properties can be used both for the reconstruction of geological processes and for the prediction of deposit location and quality as well as for specific industrial applications [7]. In particular, information about the number and types of defects is important for the processing of the raw materials and the potential technical applications.

The present study presents results of a comprehensive mineralogical and geochemical study on potential HPQ deposits of different genetic types from 10 sites in the Southern Ural region, Russia. The investigation aims to obtain detailed information about the type and abundance of lattice defects and contaminating trace elements of these quartz materials in order to determine the critical processes and conditions responsible for the formation of HPQ deposits. This aim is achieved by a combination of multiple high-sensitivity analytical techniques ranging from cathodoluminescence (CL) microscopy and spectroscopy to electron paramagnetic resonance (EPR) spectroscopy and trace-element analysis by inductively coupled plasma mass spectrometry (ICP-MS) and laser ablation ICP-MS.

2. Materials and Methods

2.1. Geological Background and Sample Material

Potential high-purity quartz from 10 different localities of the Southern Ural region northwest of Chelyabinsk (Russia) was investigated (Figure 1, Table 1). The sample material includes quartz from a pegmatite, hydrothermal quartz veins, tectonically deformed and partially recrystallized hydrothermal quartz, and quartz from two quartzite occurrences.
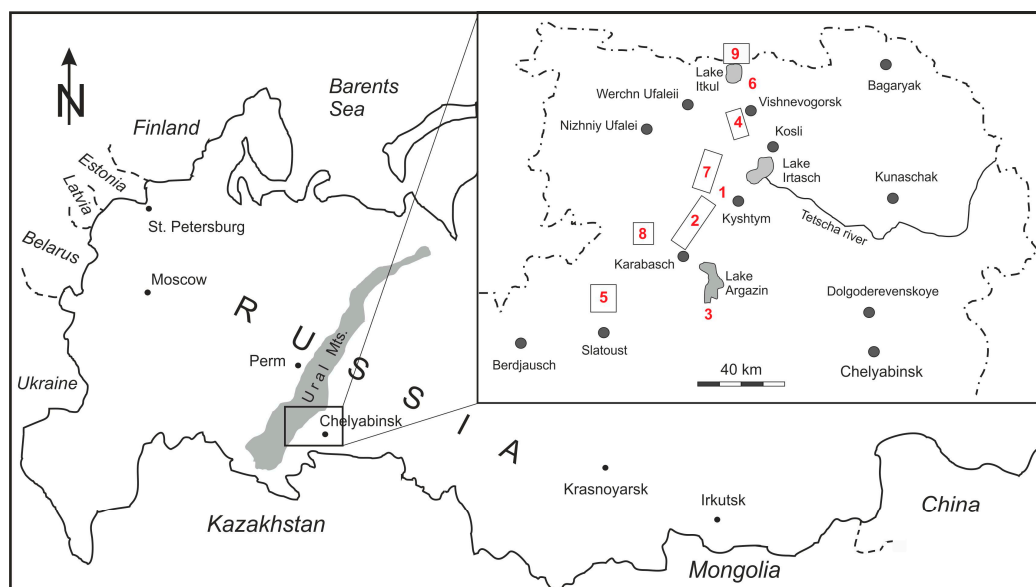

Figure 1. Topographic sketch showing the investigated quartz occurrences of the Southern Ural region northwest of Chelyabinsk (Russia); 1—Berkutinskaya (Berkut), 2—Kyshtym (sample Ky-175), 3—Argazinskoe (Arg), 4—Vjasovka (Vja), 5—Itkulskoe (Itkul), 6—Bolotnaya (Bol), 7—Kuznechikhinsk (Ku-414, Ku-2136), 8—Yurma ridge (Yur), and 9—Taganai ridge (MT-09). Numbers relate to the locations and quartz types in Table 1.

Table 1. Investigated quartz samples from the Southern Ural region (Russia).

Location	Type	Sample
1 Berkutinskaya	Pegmatite	Berkut
2 Kyshtym	Hydrothermal vein	Ky-175
3 Argazinskoe	Hydrothermal vein	Arg
4 Vjazovka	Hydrothermal vein	Vja
5 Itkulskoe	Hydrothermal vein	Itkul
6 Bolotnaya	Hydrothermal vein	Bol
7 Kuznechikhinsk	Hydrothermal vein, metamorphic overprint	Ku-414
7 Kuznechikhinsk	Hydrothermal vein, metamorphic overprint	Ku-2136
8 Yurma ridge	Quartzite	Yur
9 Taganai ridge	Quartzite	MT-09

All quartz bodies occur within the Ufalei metamorphic (gneiss–migmatite) complex, consisting of two tectonometamorphic units which lay on top of each other. Highly metamorphosed Upper Proterozoic rocks of the Ufalei suite belong to the lower unit and form the core of an anticlinorium. The hydrothermal vein deposits from Kyshtym (sample Ky-175), Kuznechikhinsk (10 km southwest of Kosli, samples Ku-414, Ku-2136), and Argazinskoe (on the southwest coast of Lake Argazin, sample Arg), and the quartzite massifs of Yurma (north of Karabasch on the Yurma ridge) as well as the Taganai ridge (north of Slatoust, sample MT-09) are situated within this unit (Table 1). The pegmatite body of the Berkutinskaya deposit is situated within the Berkut ridge near Kyschtym. The upper unit of the Ufalei metamorphic complex comprises Ordovician and Lower Devonian sequences represented by terrigenous schistose meta-sediments surrounding the anticlinorium core. This unit hosts the hydrothermal vein deposits Vjazovka near Vyschnevogorsk, Bolotnaya and Itkulskoe (north coast of Lake Itkul) (Figure 1, Table 1).

All quartz bodies were formed during long-lasting and multi-stage metamorphism in the Ural region [8]. Two main stages of metamorphism can be distinguished in the investigated area: (1) the Late Cambrian stage, which correlates with the formation of the Ufalei anticlinorium and is subdivided into two sub-stages—an early phase of progressive metamorphism (sillimanite-almandine subfacies of the amphibolite facies), followed by retrograde metamorphism; and (2) the Middle Paleozoic stage, which is characterized by metamorphic transformations of the gneiss core and schist frame (staurolite–quartz subfacies of the amphibolite facies). Silica mobilization and formation of hydrothermal quartz veins and bodies are supposedly related to the retrograde stages of both metamorphic events [9].

2.2. Analytical Methods

Polished thin sections were prepared for microscopic and cathodoluminescence (CL) investigations from all samples listed in Table 1. Polarizing microscopy was carried out using a Zeiss Axio Imager A1m (ZEISS Microscopy, Jena, Germany) to document the grain-size and microstructure of the different quartz types. Micrographs were recorded using a digital camera MRc5 and the software Axiovision (ZEISS Microscopy, Jena, Germany).

CL microscopy and spectroscopy were performed on carbon-coated thin sections using a hot-cathode CL microscope HC1-LM (LUMIC, Bochum, Germany) [10]. The system was operated at 14 kV and 0.2 mA (current density ~10 $\mu A/mm^2$) with a defocused electron beam. Luminescence images were captured during CL operations using a peltier cooled digital video-camera (OLYMPUS DP72, OLYMPUS Deutschland GmbH, Hamburg, Germany). CL spectra in the wavelength range of 370–920 nm were recorded with an Acton Research SP-2356 digital triple-grating spectrograph with a Princeton Spec-10 charge-coupled device (CCD) detector (OLYMPUS Deutschland GmbH, Hamburg, Germany) that was attached to the CL microscope by a silica-glass fibre guide. CL spectra were measured under standardized conditions (wavelength calibration by a Hg-halogen lamp, spot width 30 μm, measuring time 5 s). Irradiation experiments were performed to document the behaviour of the

quartz samples under electron irradiation. Samples were irradiated 5 min under constant conditions (14 kV, 0.2 mA) and spectra were measured initially and after every 1 min.

The paramagnetic centres of quartz-powder samples were investigated by EPR spectroscopy using a Bruker EMX spectrometer (Bruker Corporation, Billerica, MA, USA) operated with the X-band microwave frequencies at both room temperature and liquid-nitrogen temperature. Experimental conditions for room-temperature EPR included a microwave frequency of ~9.63 GHz, modulation frequency of 100 kHz, modulation amplitude of 0.1 mT, and microwave powers from 0.02 mW to 20 mW. The spectral resolutions were ~0.146 mT for wide scans 50–6500 mT and 0.024 mT for narrow scans 300–350 mT. All samples after room-temperature EPR measurements were irradiated at room temperature in a ^{60}Co cell for a dose of ~10 kGy. Low-temperature (85 K) EPR measurements were made immediately after gamma-ray irradiation, with similar experimental conditions used for the room-temperature analyses except for a microwave frequency of ~9.39 GHz.

The chemical composition of bulk quartz samples (dissolved powders) was first analysed using solution ICP-MS. The samples (400–500 mg) for ICP-MS analysis were milled to a grain size of <30 μm using a pre-cleaned agate mortar. The powdered sample was digested in a glassy carbon vessel with 5 mL concentrated HF and 3 mL concentrated HNO_3 at 50 °C (35 min). Rhenium solution (1 mL of 100 μg·L^{-1} concentration) was added as an internal standard for the ICP-MS measurements. The analysis was performed using a Perkin Elmer Sciex Elan 5000 quadrupole instrument (Percin Elmer Inc., Baesweiler, Germany) with a cross-flow nebulizer and a rhyton spray chamber. The precision and accuracy of the ICP-MS measurements were evaluated by analysis of the glass sand reference material UNS-SpS. The relative standard deviations for most analytes were below 10%. The ICP-MS results showed procedural limits of detection ranging from 0.22 μg·L^{-1} to 3.1 μg·L^{-1} for Na, Mg, Al, K, Ca and Ba. Elements such as Li, Mn and Sr had procedural limits of detection ranging from 0.02 to 0.04 μg·L^{-1}, whereas these limits range from 1 to 7 μg·L^{-1} for the other elements investigated [11].

In addition, 200-μm polished thick sections of the samples were prepared for laser ablation inductively-coupled plasma mass spectrometry (LA-ICP-MS) to determine trace elements of individual quartz crystals in situ. Concentrations of Li, Be, B, Na, Al, P, K, Ca, Ti, Mn, Fe, Ge, Rb, Sr, Ga, and Sb were analysed with a double-focusing sector field mass spectrometer ELEMENT XR coupled with a NewWave 193-nm excimer laser probe (Thermo Scientific, Waltham, MA, USA) [12]. The laser had a pulse rate of 20 Hz, a speed of 15 μm·s^{-1}, a spot size of 50 μm and energy fluence of 5–7 mJ·cm^{-2} on the sample surface. Raster ablation was applied on an area of approximately 150 μm × 300 μm. The approximate depth of ablation was about 50 μm. The carrier gas for transport of the ablated material to the ICP-MS was He mixed with Ar. External calibration was performed using three silicate glass reference materials produced by the National Institute of Standards and Technology, USA (NIST SRM 610, 612 and 614). In addition, the NIST SRM 1830 soda-lime float glass (0.1% *m/m* Al_2O_3), the certified reference material BAM No.1 amorphous SiO_2 glass from the Federal Institute for Material Research and Testing in Germany, and the Qz-Tu synthetic pure quartz monocrystal provided by Andreas Kronz from the Geowissenschaftliches Zentrum Göttingen (GZG), Germany, were used. Each measurement comprised 15 scans of each isotope, with a measurement time varying from a 0.15 s/scan for K in high resolution to a 0.024 s/scan of, for example, Li in low resolution. A linear regression model, including several measurements of the different reference materials, was used to define the calibration curve for each element. For the calculation of P concentrations, the procedure of Müller et al. [13] was applied. Ten sequential measurements on the Qz-Tu synthetic pure quartz monocrystal were used to estimate the limits of detection (LOD—3σ of 10 measurements; see Table S3). The analytical error ranges within 10% of the absolute concentration of the element.

3. Results

3.1. Cathodoluminescence (CL)

CL imaging revealed heterogeneities, intra-crystal micro-structures and micro-inclusions in the quartz samples. The detected micro-inclusions include carbonate (orange CL) in quartz from Bolotnaya, and feldspar (microcline—bright blue CL, albite—bluish-violet CL) in sample Ku-2136, as well as zircon/monazite (bright radiation halos) and mica (non-luminescent) in sample MT-09 (Figure 2).
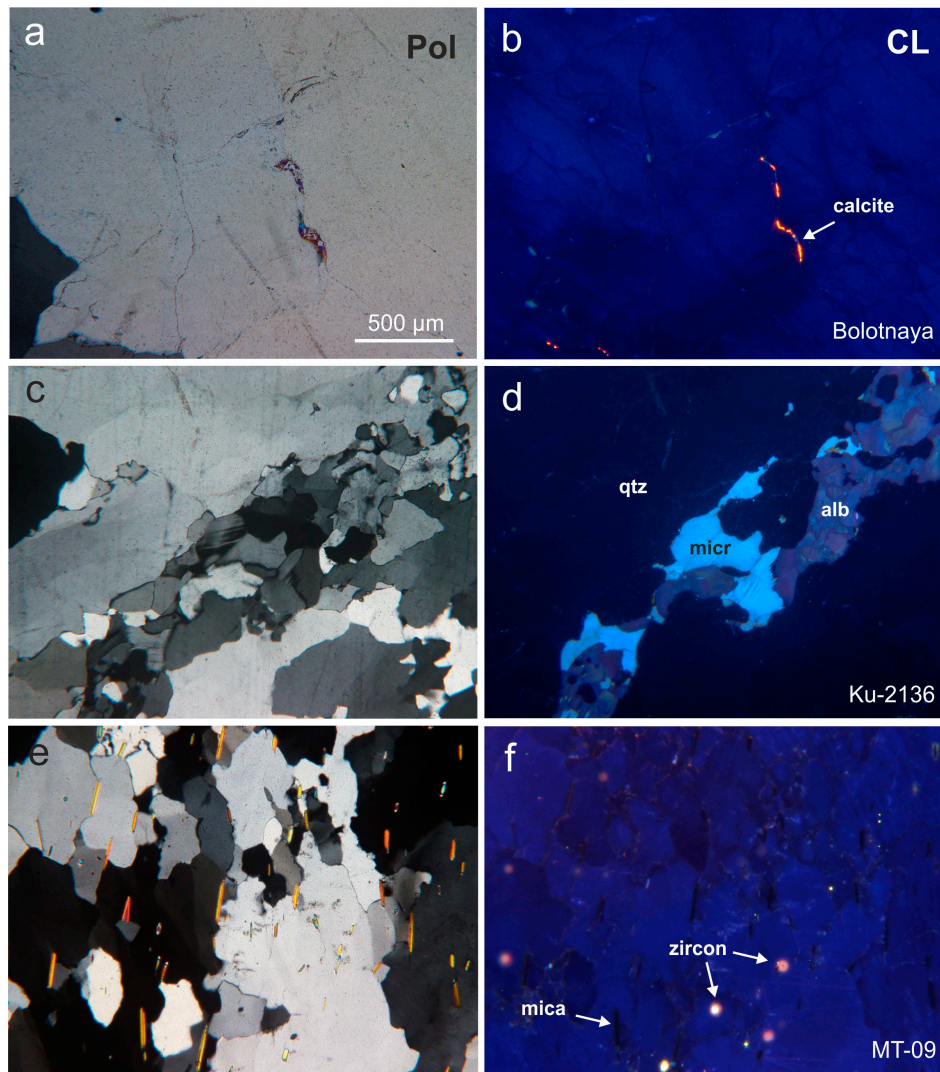

Figure 2. Micrograph pairs in transmitted light (crossed polars—Pol) and cathodoluminescence (CL) showing micro-inclusions of minerals in the quartz samples: (**a**,**b**) calcite in the hydrothermal quartz from Bolotnaya (Bolot); (**c**,**d**) microcline (micr) and albite (alb) in metamorphically overprinted hydrothermal quartz from Kuznechikhinsk (Ku-2136; (**e**,**f**) mica (non-luminescent) and zircon with radiation haloes in the quartzite from the Taganai ridge (MT-09).

The micro-inclusions can be related to the composition of the host rocks (e.g., hydrothermal carbonate veins) or the educt material of the metamorphic rocks. Heterogeneities were detected in quartz grains of almost all samples, which appeared homogeneous under polarized light. Moreover, features of alteration and recrystallization/reorganization as well as trails of fluid migration could be revealed by CL (Figure 3).
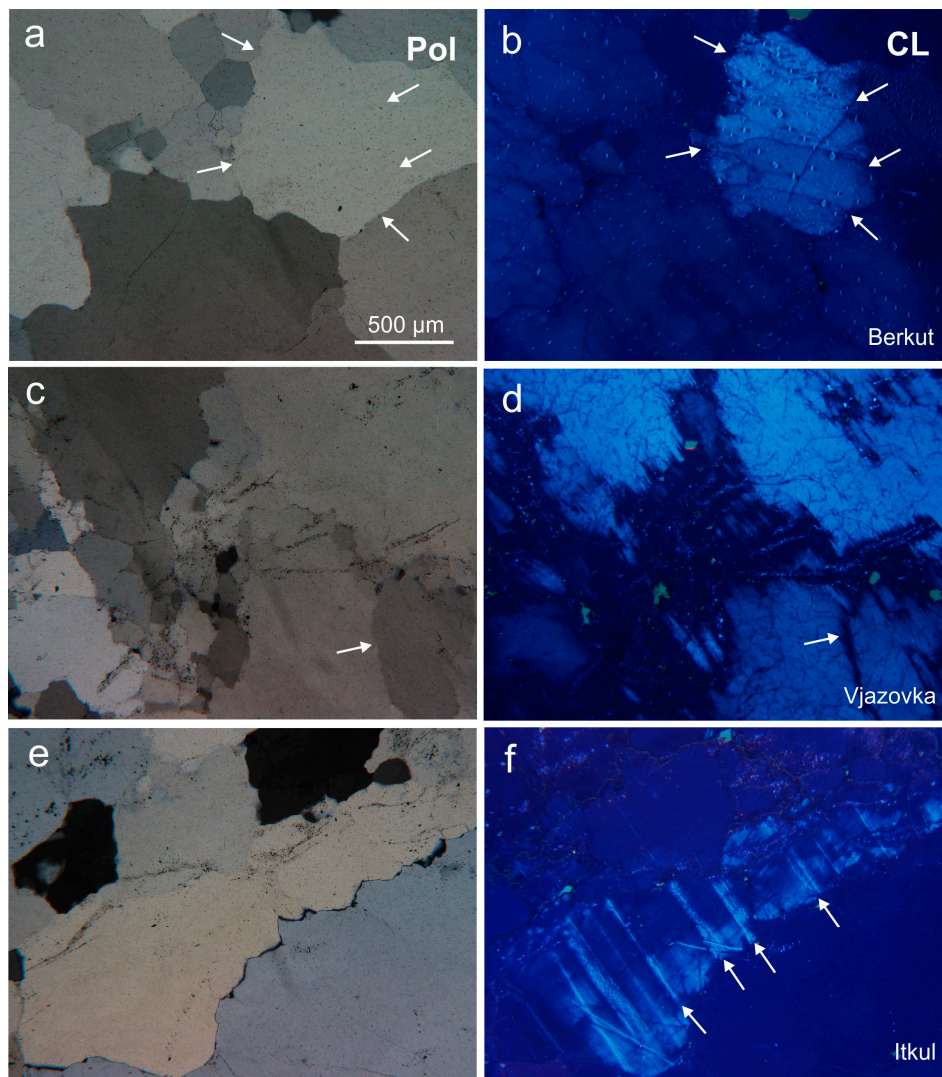
Figure 3. Examples of micro-structural heterogeneities detected by cathodoluminescence (CL) in the investigated quartz samples mostly invisible in transmitted light (crossed polars—Pol): (**a**,**b**) brightly luminescing sub-grain areas in the pegmatite quartz from Berkutinskaya (Berkut); (**c**,**d**) trails of reduced CL intensity (arrow) due to migration of fluids in the hydrothermal quartz from Vjazovka (Vja); (**e**,**f**) dislocation planes in the hydrothermal quartz from Itkulskoe (Itkul).

Pegmatite quartz shows a more or less homogeneous bluish-green CL with a characteristic CL emission band at ca. 500 nm (Figure 4a). Sub-grain areas with strong CL (Figure 3b) have the highest intensities of this 500 nm band indicating the highest amounts of the luminescence related defect(s). The intensity of the 500 nm emission strongly decreases under electron irradiation. The resulting CL spectrum after 5 min of electron bombardment consists of an emission band at 450 nm and a weak band at 650 nm (Figure 4a).
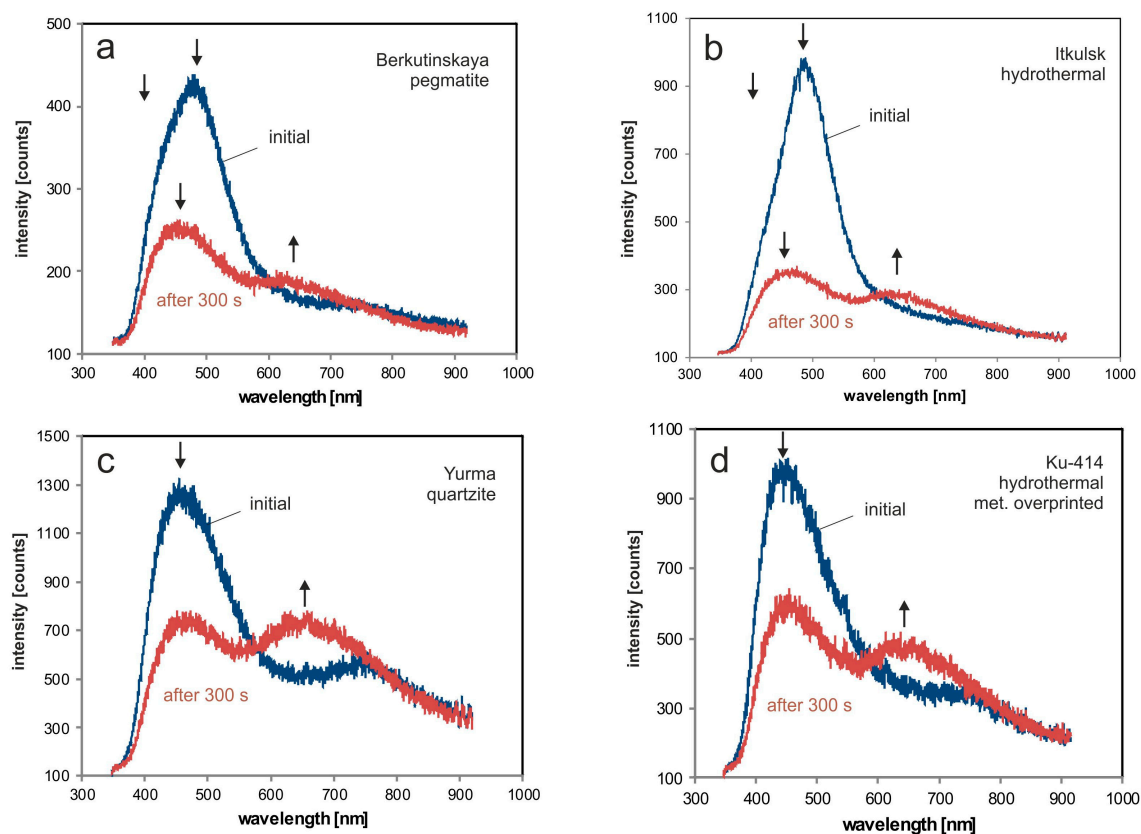
Figure 4. Representative CL emission spectra of quartz of different origin (blue spectrum = initial, red spectrum = after 5 min of electron irradiation): (**a**) pegmatite quartz; (**b**) hydrothermal vein quartz; (**c**) quartzite; (**d**) tectonically deformed and partially re-crystallized hydrothermal quartz.

Quartz from hydrothermal veins exhibits a typical short-lived blue CL. The initial spectra are mainly composed of a strong band at 500 nm and a second emission band at 390 nm, which is only visible as a shoulder (see arrow in Figure 4b) because of the spectral transmissibility of the used equipment (absorption of the spectral UV region due to glass optics). The CL spectrum after 5 min of electron irradiation is dominated by emission bands at 450 nm and 650 nm, respectively. A conspicuous feature of CL imaging in most hydrothermal quartz samples is a heterogeneous pattern (Figure 3d). Brightly luminescent areas alternate with areas of low CL intensity. Interactions of migrating fluids with the host quartz left their traces in trails of reduced CL intensities (Figure 3d). Moreover, features of deformation are visible during initial electron radiation, but disappear during electron bombardment (Figure 3f).

With increasing deformation degree of hydrothermal quartz the luminescence intensity decreases and the visible CL colour becomes more homogeneous. The typical luminescence emission bands for undeformed hydrothermal quartz at 390 nm and 500 nm are missing. The spectra of deformed hydrothermal quartz are dominated by two bands at 450 nm and 650 nm, respectively (Figure 4d).

Quartzite samples appear commonly heterogeneous under CL and may contain micro-inclusions of minerals probably originating from the primary source rocks (sample MT-09; Figure 2e,f). The quartzite from Yurma does not contain any visible mineral inclusions and represents high-purity material. Quartz from the quartzite samples is characterized by a deep blue CL showing emission bands at 450 nm and 650 nm (Figure 4c).

An orientation-dependent behaviour of the CL during electron irradiation was observed in the hydrothermal quartz from Kyshtym (Ky-175, Figure 5). Sub-grains which are cut perpendicular to the c-axis in thin section (dark in polarized light) show a change of the initial blue CL colour into red-violet

(increase of the 650 nm band), whereas sub-grains with other orientations show only a decrease of the initial blue CL (decreasing composite blue emission band).
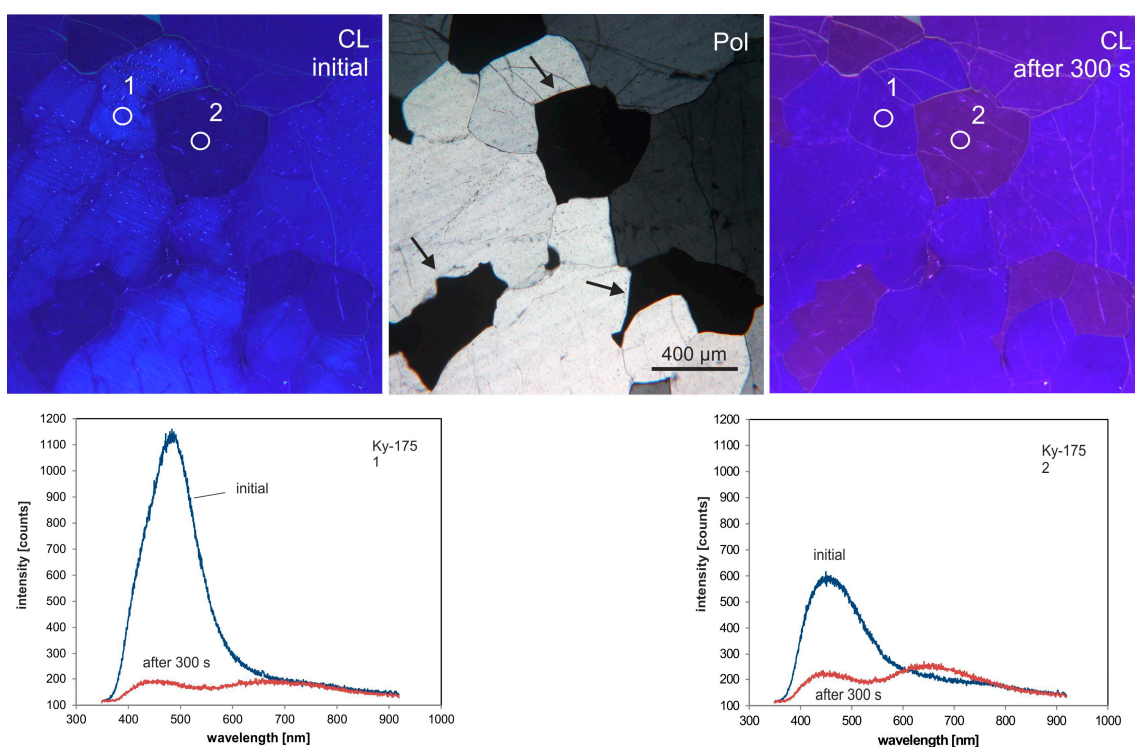

Figure 5. Micrographs in cathodoluminescence (CL) and transmitted light (crossed polars—Pol) of the hydrothermal quartz from Kyshtym (Ky-175); the images and related spectra show the initial CL and the CL after 5 min of electron irradiation. Note the different CL behaviour of quartz sub-grains with varying crystallographic orientation; sub-grains cut perpendicular to the crystallographic c-axis (see arrows) have a lower initial blue CL intensity and develop a reddish CL (650-nm emission band) due to the electron bombardment.

3.2. Electron Paramegnetic Resonance (EPR)

Figures 6 and 7 present the EPR spectra of all quartz samples measured at room temperature. The EPR spectra are essentially featureless, except for the presence of trace and variable amounts of the rhombic Fe^{3+} signal at the effective g value of ~4.38 (Figure 6) [14,15].
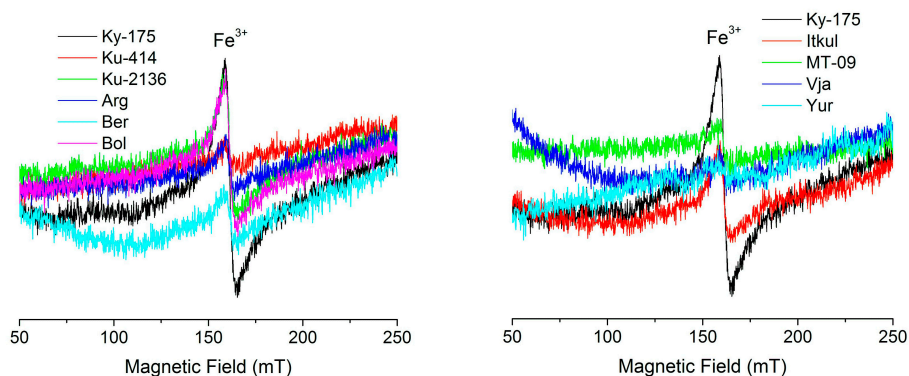

Figure 6. Electron paramagnetic resonance (EPR) spectra of investigated quartz samples taken at room temperature showing the weak rhombic Fe^{3+} signal at g_{eff} = 4.38; the intensities are given in arbitrary units.

Obviously, the intensity of this signal is low in all samples (i.e., low signal-to-noise ratios) and is variable between samples. Even without a proper standard, it is apparent that the Fe^{3+} signal is exceedingly small in the samples Berkutinskaya (pegmatite), Argazinskoe, Vjasovka (hydrothermal veins), Ku-414 (metamorphically overprinted hydrothermal quartz), MT-09, and Yurma (quartzite). The Fe^{3+} signal is somewhat more elevated in the samples Ky-175, Itkulskoe, Bolotnaja (hydrothermal vein), and Ku-2136 (metamorphically overprinted hydrothermal quartz).

The spectra in Figure 7 show the resonance signals at the central magnetic field region. Again, all spectra have low signal-to-noise ratios. Indeed, none of the radiation-induced defects at the effective g values of ~2.00 are present [16–19]. Even the common E'_1 is exceedingly rare. It should be mentioned that the silica tubes used as sample containers show a very weak E'_1 signal, which contributes to the weak E'_1 signal in the measured spectra (Figure 7).
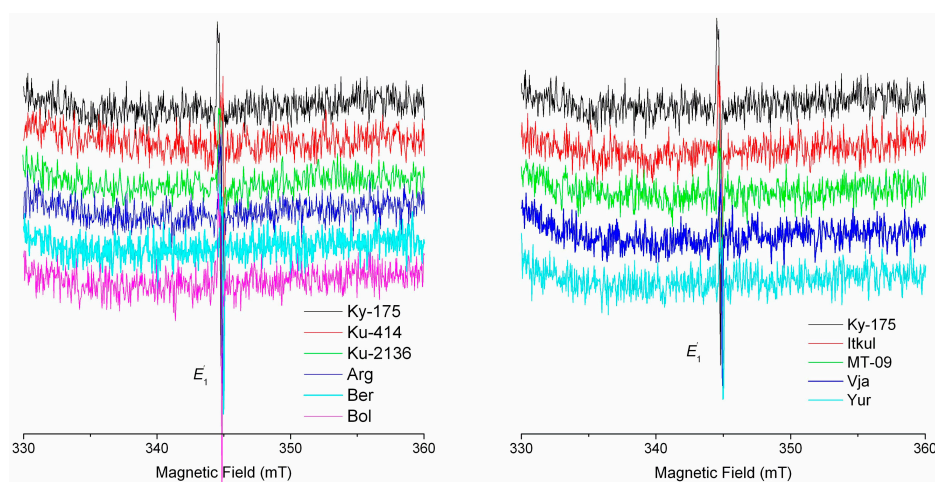

Figure 7. EPR spectra of investigated quartz samples taken at room temperature showing a slight E'_1 but a general absence of other radiation-induced defects at $g_{eff} = 2.0$.

The EPR spectra of gamma-ray-irradiated samples, measured at 85 K, all show the presence of varying amounts of the well-known $[AlO_4]^0$ centre with the characteristic ^{27}Al hyperfine structure [20] (Figure 8). The paramagnetic $[AlO_4]^0$ centre in quartz has been shown to form from neutral $[AlO_4/M^+]^0$ (M = H, Li, Na, K) precursors (i.e., the monovalent charge compensators migrated away during room-temperature irradiation) [20,21]. Figure 8 compares the individual spectra using the sample Ky-175 as a common reference. The intensities of measured $[AlO_4]^0$ signals of samples Argazinskoje, Bolotnaya and Yurma are notably higher than those of the other samples.
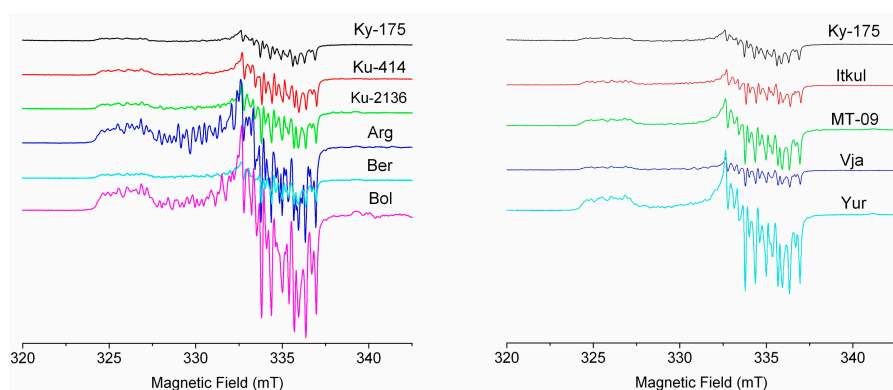

Figure 8. EPR spectra of investigated quartz samples taken at 85 K showing varying quantities of the $[AlO_4]^0$ centre.

EPR spectra measured at 85 K show again the presence of the Fe^{3+} and the E'_1 centre but a general absence of the Ti- and Ge-associated defects with diagnostic ^{47}Ti, ^{49}Ti and ^{73}Ge hyperfine structures [16,19], confirming the results observed at room temperature.

3.3. Trace Elements

"Bulk" solution ICP-MS: Trace-element concentrations of all investigated quartz samples determined by solution ICP-MS are summarized in Tables S1 and S2. The data illustrate that most quartz samples have low concentrations of most trace elements compared with average concentrations in natural quartz [5,7]. Al concentrations are generally below 100 ppm, and those of Fe and Ti are below 10 ppm. An exception is the quartzite from the Taganai ridge (sample MT-09) which shows elevated concentrations of Al, K, Mg, Ti, Fe, Mn, Zr, U, Th, and Hf. Based on microscopic investigations the elevated concentrations of Al, K, Mg, Ti, Fe and Mn are caused by micro-inclusions of mica and those of Zr, U, Th and Hf by zircon (Figure 2e,f). There are similar effects of micro-inclusions of feldspars (albite, microcline—Figure 2d) in quartz from Kuznechikhinsk (samples Ku-2136—K, Na, Al and Fe) as well as carbonate (Figure 2b) in the sample from Bolotnaja (sample Bolot—Ca, Mg and Fe).

Sodium, Sr, K, Mg, and Rb show positive correlations in the different samples (Figure 9). The abundance of these alkali and alkali earth elements can predominantly be related to the presence of fluid inclusions, although mineral micro-inclusions of feldspar and mica (e.g., samples MT-09, Ku-2136) can also influence these correlations. However, in most of the investigated quartz no mineral inclusions were detected.
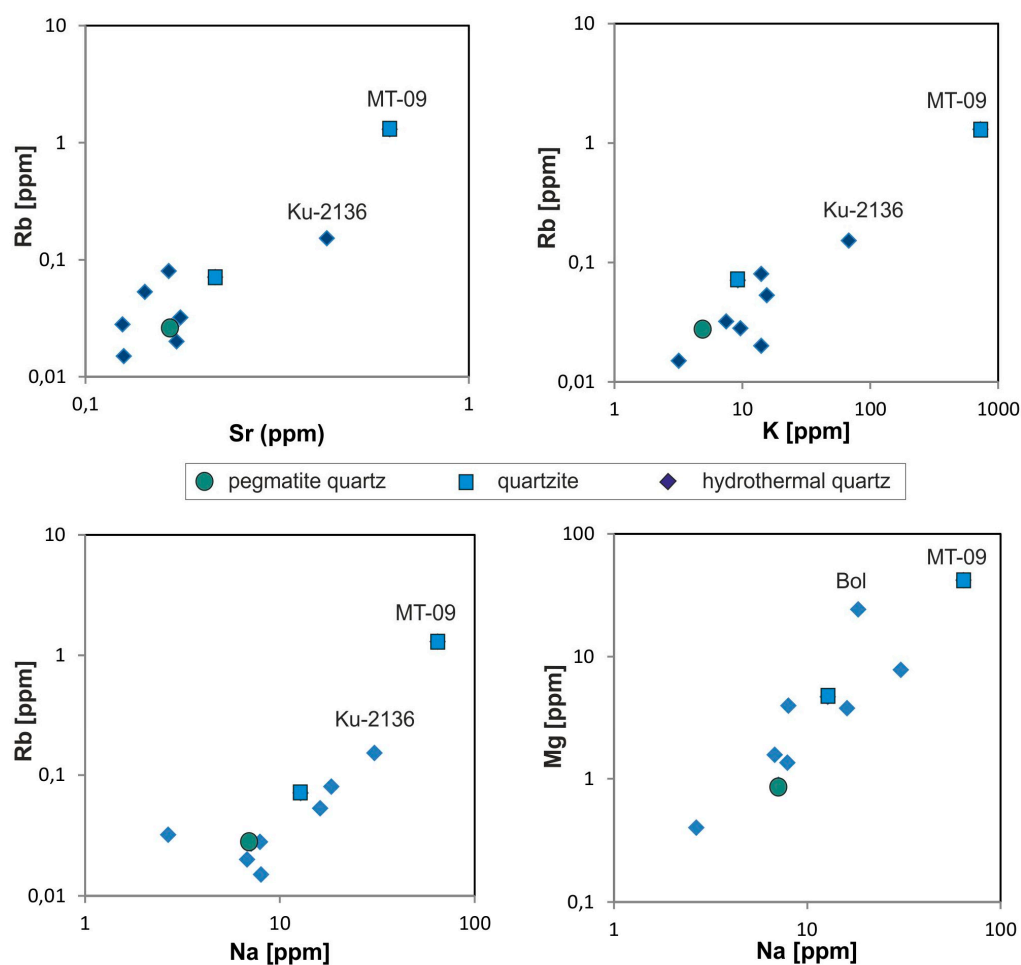

Figure 9. Element ratios of selected alkali and alkali earth elements in the investigated quartz samples (the labelled samples are those with detected mineral inclusions).

The rare earth element (REE) concentrations are listed in Table S2 and illustrated in Figure 10. In some samples (Berkutinskaya, Bolotnaya, Ku-414, and Ku-2136) the concentrations of certain rare earth elements are below the detection limit of the applied ICP-MS analysis and, thus, their chondrite-normalized REE distribution patterns are not shown in Figure 10. The REE patterns of the two quartzite samples are different to the patterns of the hydrothermal quartz. In particular, the quartzite sample MT-09 has high absolute REE concentrations with a typical crustal signature of enriched light REE (LREE) and depleted heavy REE (HREE) (Figure 10a). The REE enrichment is most likely be related to micro-inclusions found in this sample. The quartzite from Yurma has much lower REE contents but shows a similar LREE pattern. However, the HREE are slightly enriched.
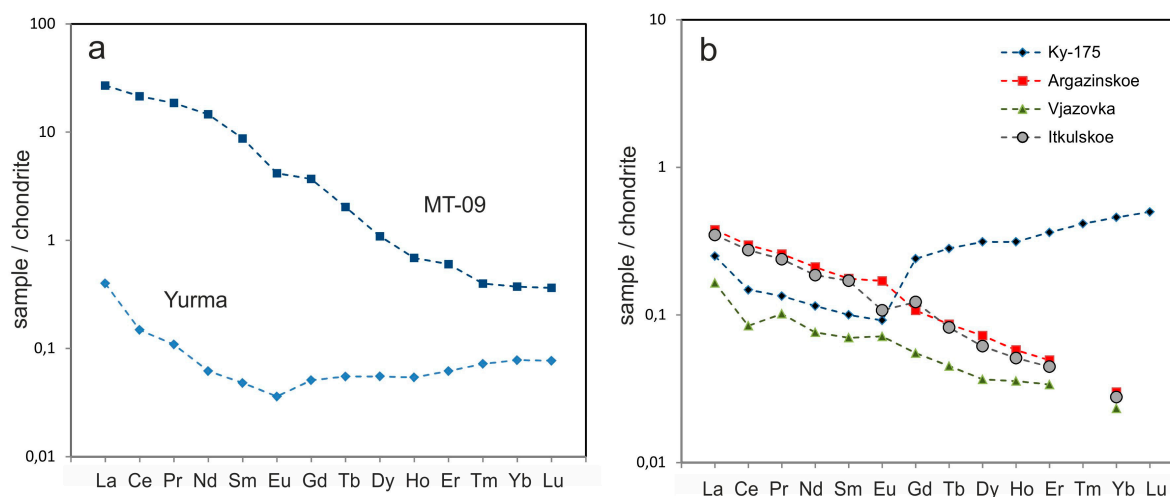

Figure 10. Chondrite-normalized rare earth element (REE) distribution patterns of quartzite (**a**) and hydrothermal vein quartz (**b**) (normalization according to data of Anders and Grevesse [22]).

Three of the hydrothermal quartz samples (Argazinskoe, Vjasovska, Itkulskoje) are similar both in absolute REE values and in their chondrite-normalized REE patterns, which correspond to the common crustal distribution (Figure 10b). Only a slight negative Ce anomaly (Vjazovka) and negative (Itkulskoe) or positive (Argazinskoe, Vjazovka) Eu anomalies are detectable. Quartz Ky-175 shows comparable LREE patterns but steeply increasing HREE (Figure 10b), which is most likely caused by zircon or xenotime micro-inclusions.

Summarizing, the "bulk" solution ICP-MS provides concentrations of lattice-bound trace elements plus concentrations of elements bound in mineral and fluid micro-inclusions, which could not be removed during sample preparation.

In situ LA-ICP-MS: Element concentrations determined by in situ LA-ICP-MS are generally lower than those determined with solution ICP-MS, except Ge, Ti and Li (Tables S1 and S3). This is mainly due to the fact that during laser ablation the analyses of visible (>0.5 μm) micro-inclusions can be avoided by choosing clear, inclusion free ablation areas. Thus, concentrations measured by LA-ICP-MS reflect almost the values of lattice-bound trace elements.

Aluminium concentrations analysed by LA-ICP-MS are consistently low (<15 ppm) for all samples except sample Vjazovka (from 21 to 32 ppm). Titanium has more variable concentrations (compared with its general abundance in quartz, e.g., [5]), ranging from <1 ppm to 37 ppm. Lithium concentrations are very low in all samples (<2.3 ppm). Boron and Ge were also found in low concentrations, except in the sample Argazinskoe, which has up to 5.3 ppm B and 1.6 ppm Ge. The Berkutinskaya sample (pegmatite quartz) has high P concentrations, of up to 7.6 ppm.

4. Discussion

4.1. Trace Element Incorporation Into Quartz

The applied combination of CL, EPR and ICP-MS methods permits the identification of types of structural defects and provide insights into their incorporation and/or transformation mechanisms during quartz crystal genesis. In addition, the results provide first indications concerning the very low trace-element concentrations and show the potential of the sampled quartz deposits for high-purity applications in the industry. These data are essential for the prediction of theoretical limits of the processing procedure, assuming that impurities from mineral and fluid inclusions could be minimized or completely removed during refinements.

Figure 11 shows the concentrations of Al and Ti measured by laser ablation ICP-MS (LAICP-MS) and the field defining the quartz economically as high-purity quartz (HPQ) in accordance with Harben [3] and Müller et al. [4]. It can be concluded that all quartz samples except MT-09 plot into the HPQ field. The best chemical quality is of quartz of the hydrothermal veins at Kyshtym (Ky-175) and Itkulskoe.
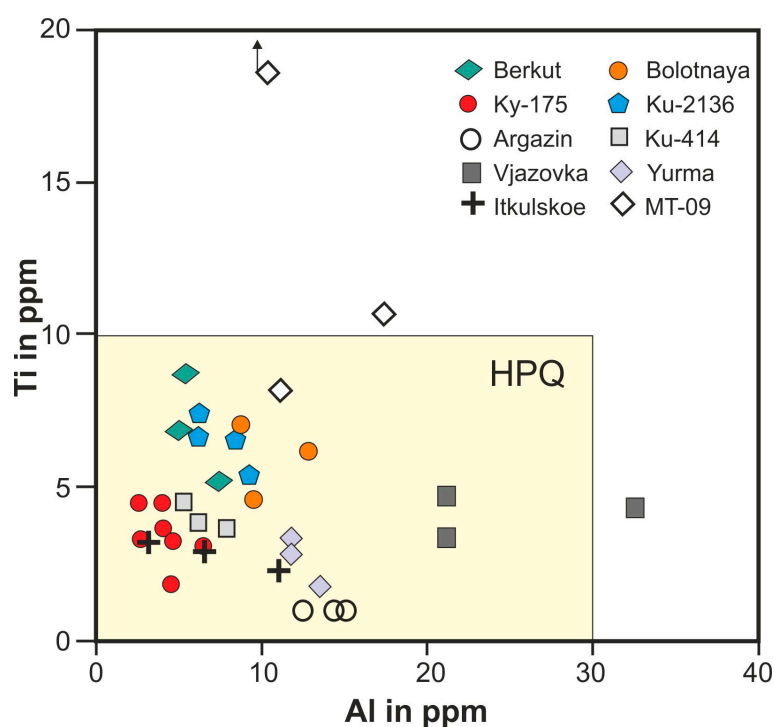

Figure 11. Ti and Al concentrations from laser ablation inductively-coupled plasma mass spectrometry (LA-ICP-MS) analyses of the quartz samples plotted into the field of high-purity quartz (HPQ) according to Harben [3] and Müller et al. [4].

Some elements (Ge, Ti, Li) show more or less constant concentrations when comparing the data from solution ICP-MS analyses of bulk quartz and LA-ICP-MS measurements of selected inclusion-free areas. For these elements it can be concluded that they are preferentially incorporated in the quartz structure. Because of the very low concentrations of these elements no EPR signals were detectable for potential paramagnetic defects.

In contrast to the above mentioned elements, Al concentrations measured by LA-ICP-MS are much lower than those analysed in the bulk quartz by ICP-MS. Although the EPR data show that the paramagnetic $[AlO_4]^0$ centre is the most frequent in the investigated quartz; not all of the Al measured by solution ICP-MS seems to be structurally bound. The paramagnetic $[AlO_4]^0$ centre and its diamagnetic precursors $[AlO_4/M^+]^0$ play an important role as imperfections in quartz. The monovalent

ions H^+, Li^+, Na^+ commonly charge-compensate the Al defects. However, Na (together with other alkali and alkali earth elements) seems to be mainly related to fluid inclusions (see Figure 9) and the Li content is low in all samples. Data from literature show that hydrothermal quartz mineralization and pegmatite quartz often contain elevated concentrations of Li [23], and Li is a common charge-balancing cation for Al [24]. The data of the present study, however, indicate that the charge compensator of Al^{3+} substituting Si^{4+} is predominantly H^+. This is in accordance with the results of Miyoshi et al. [25] who detected a preferred incorporation of H^+ as the charge-balancing cation of Al defects in hydrothermal quartz. Müller et al. [26] have already shown that igneous quartz preferentially incorporates H^+ as a charge-balancing cation in lieu of Li, K and Na. Similar findings have been made more recently for pegmatite quartz [27,28].

Although the comparison of EPR and trace-element data reveals a general trend of an increasing number of paramagnetic Fe centres with increasing contents of chemically measured Fe concentrations (with the exception of sample MT-09), there are nevertheless variations in the absolute values. The differences could be explained by two different facts. First, Fe-bearing micro-inclusions are the reason for elevated Fe concentrations in the bulk quartz samples. This is especially true for sample MT-09, where a couple of mineral inclusions (e.g., mica) have been detected by microscopy. Second, Fe is known to occur as both Fe^{2+} and Fe^{3+} in quartz [15,29]. However, Fe^{2+} is not detectable by EPR at X-band frequencies [14]. Therefore, 1:1 correlations of the Fe^{3+} EPR signal with the total Fe contents from chemical analyses are not expected.

4.2. Cathodoluminescence and Structural Defects

Characteristic luminescence colours of quartz with different geological history, and associated spectral CL measurements together with the results from the EPR spectroscopy provided information about the defect structures and incorporated trace elements, primary growth conditions, and processes of secondary overprint. These features not only influence the properties and quality of the potential quartz raw material, but also allow insights into the genetic history of the quartz occurrences.

According to Ramseyer and Mullis [30] and Götze et al. [31] the activation of the visible greenish-blue CL of the pegmatite quartz from Berkutinskaya is associated with cation compensated trace-element centres in the quartz structure. The intensity of the luminescence emission falls off rapidly after electron bombardment within 30–60 s, which can be related to ionization-enhanced diffusion of luminescence centres as was shown by Ramseyer and Mullis [30] with electro-diffusion experiments. However, the absolute concentration of Al in this sample is low (<10 ppm). This is confirmed by the low abundance of paramagnetic trace-element defects of Al, Ti and Ge. Also, the contents of Li and other cations are far below the common abundance of such elements in pegmatite quartz [24,31]. The heterogeneous CL textures of grains indicate a heterogeneous distribution of trace elements responsible for the CL (Figure 3b). Only areas with higher intensity (brighter CL) of the transient CL point to elevated contents of responsible trace elements (e.g., Al, Li). Moreover, a possible role of H^+ for the 500-nm luminescence signal must be taken into consideration.

All hydrothermal quartz samples show a characteristic short-lived blue CL, which is elicited by two main emission bands at ~390 nm and 500 nm. According to Ramseyer and Mullis [30] and Perny et al. [32] these luminescence bands are activated by cation-compensated $[AlO_4/M^+]$-centres in the quartz structure. The strong decrease of these emission bands during electron irradiation is due to the interaction of the cation-balanced Al centres with the electron beam and indicates elevated trace element contents in areas with high CL intensity [30,33] (Figure 4b). Such heterogeneous pattern is depicted in the quartz from Vjazovka (compare Figure 3d), which has an elevated concentration of Al compared to the other samples but shows no remarkable EPR signal for the $[AlO_4]^0$ centre.

The relatively low contents of Al and charge-balancing cations in some of the investigated hydrothermal quartz suggest that either the $[AlO_4/M^+]$ defects are effective CL activators (i.e., even low abundance of $[AlO_4/M^+]$ can activate the characteristic CL), or that other activators exist for this specific luminescence. Gorton et al. [34] found the typical short-lived blue CL in synthetic

quartz with extremely low impurity concentrations and concluded that probably other activators than [AlO$_4$/M$^+$]-defects might be additionally responsible for the blue CL. However, the EPR measurements in the present study did not provide any indication for other luminescence-active paramagnetic defects. EPR measurements revealed an almost complete absence of intrinsic lattice defects associated with oxygen or silicon vacancies (e.g., the E' centre, O$_2$$^{3-}$ centre), and even the abundance of paramagnetic trace-element defects of Al, Ti, Ge is in general low.

Areas of dull CL in hydrothermal quartz can be the result of post-crystallization overprint. For instance, the interaction of migrating fluids with the host quartz left their traces in trails of reduced CL intensity (Figure 3d). Van den Kerkhof and Hein [35] explained this phenomenon with the loss of trace elements during recrystallization of the interacting area with the fluids. Decreased luminescence intensities were also detected along grain boundaries. This can probably be related to the opening of fluid inclusions and the migration of inherited fluids (especially along grain boundaries).

Indications of secondary overprint and deformation are also visible in features of apparent dislocation planes (Figure 3f). Supplementary electron back scattered diffraction (EBSD) measurements provided evidence of Dauphine twinning, which is preferentially initiated by mechanical deformation. In addition, these analyses revealed low-angle tilting of sub-grains due to deformation (Figure 12).
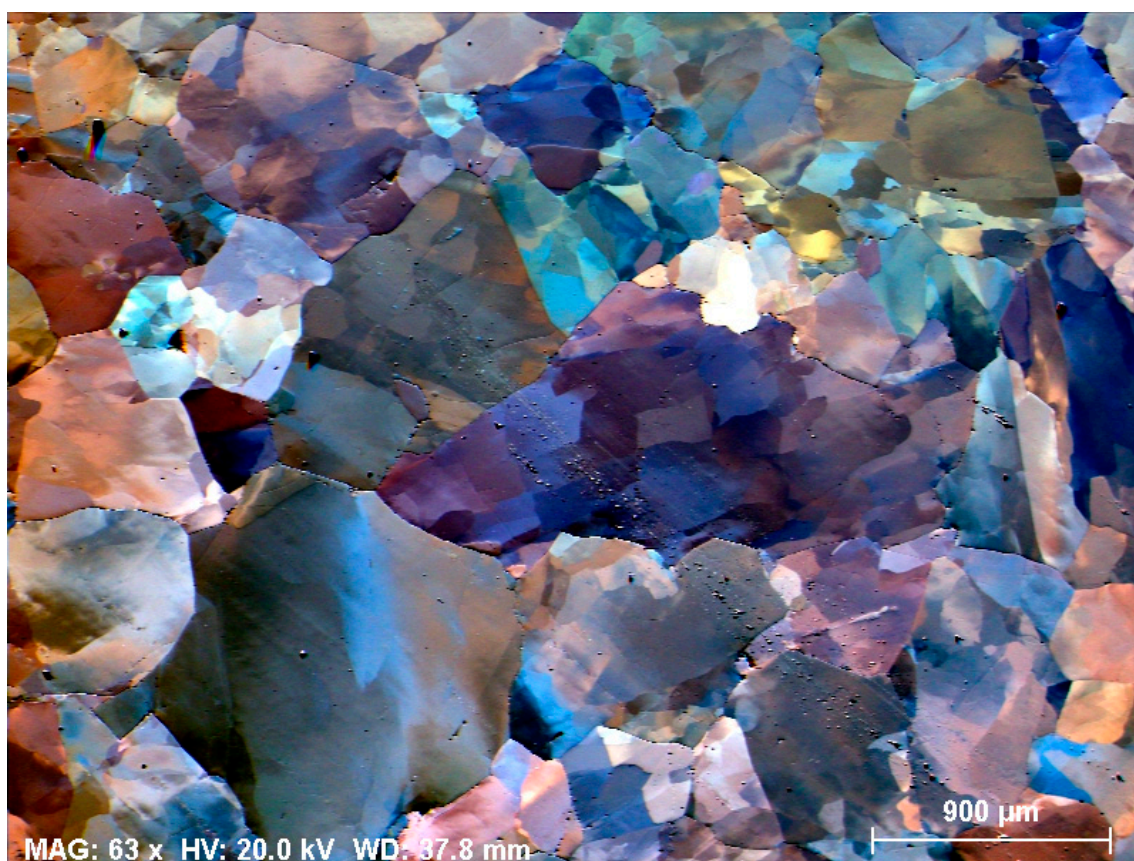

Figure 12. SEM forescattered image showing low-angle tilting of sub-grains due to deformation in the hydrothermal quartz from Kyshtym (Ky-175).

The quartz samples from Kuznechikhinsk (Ku-414, Ku-2136) illustrate that deformation of hydrothermal quartz resulted in a general decrease of the luminescence intensity and a homogenization of the CL pattern. This fact can probably be related to healing of defects and reduction of trace-element impurities due to recrystallization and reorganization processes of the quartz lattice. Measured trace-element contents are low (e.g., Al < 10 ppm, Ti < 2 ppm, Li ~1 ppm) and even the detected intensities of paramagnetic defects of Al and Fe as well as vacancy-related defects are very low.

The visible CL colour of both metamorphically overprinted hydrothermal quartz and quartzite is dark blue, and the spectra are dominated by two bands at 450 and 650 nm, respectively (Figure 4c,d). The typical luminescence emission bands at 390 nm and 500 nm that were detected in the hydrothermal quartz samples are missing. The emission observed at ~450 nm is associated with O-deficiency centres (ODC) in quartz [36,37]. It can be related to the recombination of the self-trapped exciton (STE), which involves an irradiation-induced oxygen Frenkel pair consisting of an oxygen vacancy and a peroxy linkage [38].

The 650-nm emission is attributed to non-bridging oxygen-hole centres (NBOHC), which are formed from different precursor defects [39,40]. A number of different precursors of this NBOHC have been proposed, such as H- or Na-impurities, peroxy linkages (O-rich samples), or strained Si-O bonds [38]. The time dependent spectra reveal an increase of the 650 nm band under the electron beam, which points to a conversion of precursor centres into the NBOHC. Considering the mechanical deformation of the samples, strained Si–O bonds may result in bond breaking during electron bombardment and thus, in the formation of NBOHC and the related increase of the 650-nm emission band.

Another conspicuous CL feature is the orientation-dependent CL behaviour that was observed in the hydrothermal quartz from Kyshtym (sample Ky-175; Figure 5). The initial blue CL colour of quartz sub-grains cut perpendicular to the crystallographic c-axis turned into a red-violet CL colour during electron irradiation (due to increasing 650-nm emission intensity). Surprisingly, sub-grains with other orientations do not show the same effect and only the intensity of the initial blue CL decreases (strong decline of the 450-nm emission band).

It cannot be ruled out that the crystallographic orientation of the crystals influences the interaction with the electron beam due to the relatively open structural channels along the c-axis of the quartz lattice. An alignment of the c-axis along the microscope axis would than provide a more intensive interaction with the electron beam, i.e., an increased conversion of precursor centres of the NBOHC associated with a stronger increase of the 650-nm emission. Another explanation is probably the influence of polarization effects of the luminescence light. Walderhaug and Rykkje [41] compared c-axis orientations of quartz grains and related CL colours and found clear indications that the observed colour variations are a function of crystallographic orientation. They concluded that this might be due to selective absorption of light along different crystallographic directions, a phenomenon well known from spectroscopy. Sippel [42] reported similar effects of the quartz CL when observing the luminescence under a nicol prism. The quartz CL showed strong polarization effects with variations of the CL colour from red to blue through a rotating polarizer. He found that the blue oscillators are aligned with the c-axis, whereas the red emission is unpolarized. Such a behaviour might explain the observed colour variations in the investigated quartz sample Ky-175. The effect may be interpreted by anisotropic luminescing centres that have oriented the oscillation in a strong internal crystal field.

4.3. Genetic Implications for the Formation of High-Purity Quartz

The investigated quartz localities in the northern Ural were all formed during multiple metamorphism and related deformation. According to Kelman [9], silica mobilization and formation of quartz veins and bodies can especially be related to the retrograde stage of the two metamorphic events. Although quartz from the different locations may originate from varying processes, all types show in general low concentrations of trace elements and low abundance of other point defects. Elevated trace-element contents in several samples can unambiguously be related to micro-inclusions (e.g., samples MT-09, Ku-2136).

The low abundance of structural point defects such as E'_1 centres in the quartz samples investigated requires a combination of the following two conditions: (1) low intrinsic structural imperfection (i.e., low oxygen and silicon vacancies); and (2) weak natural irradiation. This fact implies that there was sufficient time for crystallization under more or less equilibrium conditions during the formation of these quartz occurrences. On one hand, the metamorphic processes caused

the mobilization of silica-rich fluids (hydrothermal veins) and melts (pegmatite), and the precipitation as high-purity quartz. On the other hand, recrystallization, healing of defects or disintegration of fluid inclusions under metamorphic conditions resulted in a natural "purification" of the pre-existing quartz crystals and a lowering of trace-element contents. Larson et al. [43] and Müller et al. [5] found that Li concentrations in quartz can be reduced during recrystallization, and Al contents may both decrease or increase depending on the specific environment. Germanium and Ti seem to be more or less unchanged.

The formation of such metamorphic mobilisates appears to be an appropriate process for the formation of HPQ deposits. Compared with data from the literature, the analysed absolute trace-element concentrations as well as chondrite-normalized REE distribution patterns are similar to those of metamorphic and hydrothermal quartz from other regions [44]. Even the pegmatite quartz from Berkutinskoe (Berkut) follows this trend, with atypical very low concentrations of characteristic elements for pegmatite quartz such as Al, Ge or Li.

The REE patterns mostly show a crustal signature indicating a source of the silica from mobilization processes of crustal material. Only the hydrothermal quartz from Kyshtym (Ky-175) has elevated concentrations of HREE. This unusual pattern is most likely caused by zircon or xenotime micro-inclusions.

In conclusion, the results of the present study show a strong link between metamorphic processes and formation of quartz bodies of high purity. If the quartz bodies are large enough and the abundance of pre- and syn-genetic micro-inclusions is low, they may represent potential HPQ deposits.

5. Conclusions

The investigation of quartz samples of different genetic types (hydrothermal, pegmatite, and quartzite) from 10 localities in the Southern Ural region (Russia) using an analytical combination of CL microscopy and spectroscopy, EPR spectroscopy, and bulk as well as spatially resolved trace-element analysis, proved to characterize the type and abundance of trace elements and structural defects in quartz, and reconstruct processes responsible for their formation. In situ LA-ICP-MS analysis showed cumulative trace-element concentrations of <50 ppm with <30 ppm Al and <10 ppm Ti for almost all samples, defining the quartz economically as high-purity quartz. EPR data confirmed the low abundances of substitutional Ti and Fe and showed Al to be the only significant trace element structurally bound in the investigated quartz samples. Elevated concentrations of selected trace elements that were analysed with "bulk" solution ICP-MS could be related to mineral (Ti, Al, Fe, Mn, Mg, K, Zr, U, Th, Hf) and fluid (Na, K, Rb, Ca, Mg, Sr) micro-inclusions.

CL imaging reveals a heterogeneous distribution of luminescence centres, i.e., varying amounts of activator trace elements in the quartz grains. Hydrothermal and pegmatite quartz exhibit a distinct short-lived greenish-blue CL with main CL emission bands at ~390 and 500 nm, which can be attributed to $[AlO_4/M^+]$ (M = H, Li, Na, K) defects. Low contents of Li, Na and K indicate that H^+ is the main charge-balancing cation of Al^{3+}-related defects. Accordingly, areas with bright greenish-blue CL could be related to higher abundances of the $[AlO_4/M^+]$ defects. Moreover, an orientation-dependent behaviour of the CL during electron irradiation was observed that can be related to anisotropy effects of the crystal lattice, which results in an orientation-dependent interaction with the electron beam and the selective absorption of emitted light along different crystallographic directions.

Certain features of alteration, recrystallization/reorganization as well as trails of fluid migration revealed by CL in the quartz samples can be related to metamorphism-related deformation. All quartz bodies were formed during retrograde stages of complex metamorphic processes, resulting in silica mobilization and formation of quartz veins and lenses. Deformation of hydrothermal quartz resulted in a general decrease of the luminescence intensity and a homogenization of the CL pattern. This feature can probably be related to healing of defects and reduction of trace-element impurities due to recrystallization and reorganization processes of the quartz lattice. The geochemical and spectroscopic data demonstrate that the formation of such metamorphic mobilisates is an appropriate process for

the formation of high-purity quartz (HPQ) deposits. Also, the quartz occurrences formed prior to the metamorphic events (pegmatite, quartzites) were suggestively purified during regional metamorphism and deformation, resulting in a high-purity quartz province in the Southern Urals.

Author Contributions: Jens Götze and Elena Kotova conceived and designed the experiments; Elena Kotova provided the sample material; Jens Götze, Yuanming Pan, Axel Müller, Elena Kotova, and Daniele Cerin performed the experiments; Jens Götze, Yuanming Pan and Axel Müller analysed the data; Jens Götze wrote the paper.

Conflicts of Interest: The authors declare no conflict of interest.

References

1. Heaney, P.J.; Prewitt, C.T.; Gibbs, G.V. Silica—Physical Behaviour, Geochemistry and Materials Application. In *Reviews in Mineralogy*; Mineralogical Society of America: Washington, DC, USA, 1994; Volume 29, p. 606, ISBN 0-939950-35-9.

2. Götze, J.; Möckel, R. *Quartz: Deposits, Mineralogy and Analytics*; Springer: Berlin/Heidelberg, Germany, 2012; p. 360, ISBN 978-3-642-22161-3.

3. Harben, P.W. *The Industrial Mineral Hand Book—A Guide to Markets, Specifications and Prices*, 4th ed.; Industrial Mineral Information: London, UK, 2002; p. 412, ISBN 978-1900663519.

4. Müller, A.; Ihlen, P.M.; Wanvik, J.E.; Flem, B. High-purity quartz mineralisation in kyanite quartzites, Norway. *Miner. Depos.* **2007**, *42*, 523–535. [CrossRef]

5. Müller, A.; Wanvik, J.E.; Ihlen, P.M. Petrological and chemical characterization of high-purity quartz deposits with examples from Norway. In *Quartz: Deposits, Mineralogy and Analytics*, 1st ed.; Götze, J., Möckel, R., Eds.; Springer: Berlin/Heidelberg, Germany, 2012; pp. 71–118.

6. Müller, A.; Ihlen, P.M.; Snook, B.; Larsen, R.; Flem, B.; Bingen, B.; Williamson, B.J. The chemistry of quartz in granitic pegmatites of southern Norway: Petrogenetic and economic implications. *Econ. Geol.* **2015**, *110*, 137–157. [CrossRef]

7. Götze, J. Chemistry, textures and physical properties of quartz—Geological interpretation and technical application. *Mineral. Mag.* **2009**, *73*, 645–671. [CrossRef]

8. Melnikov, E.P. Main controlled factors of localization of the granulated quartz in the Southern part of the Ufaleisky anticlinorium. In *Vein Quartz of the Eastern Hang of the Urals*; Melnikov, E.P., Melnikova, N.I., Eds.; Nedra: Moscow, Russia, 1970; Issue No. 80, pp. 41–50. (In Russian)

9. Kelman, G.A. *Migmatite Complexes of the Mobile Belt*; Nedra: Moscow, Russia, 1974; p. 191. (In Russian)

10. Neuser, R.D.; Bruhn, F.; Götze, J.; Habermann, D.; Richter, D.K. Kathodolumineszenz: Methodik und Anwendung. *Zent. Geol. Paläontologie Teil I* **1995**, *H 1*, 287–306.

11. Monecke, T.; Bombach, G.; Klemm, W.; Kempe, U.; Götze, J.; Wolf, D. Determination of trace elements in the quartz reference material UNS-SpS and in natural quartz samples by ICP-MS. *Geostand. Newsl.* **2000**, *24*, 73–81. [CrossRef]

12. Flem, B.; Müller, A. In situ analysis of trace elements in quartz using Laser ablation inductively coupled plasma mass spectrometry. In *Quartz: Deposits, Mineralogy and Analytics*, 1st ed.; Götze, J., Möckel, R., Eds.; Springer: Berlin/Heidelberg, Germany, 2012; pp. 219–236.

13. Müller, A.; Wiedenbeck, M.; Flem, B.; Schiellerup, H. Refinement of phosphorus determination in quartz by LA-ICP-MS through defining new reference material values. *Geostand. Geoanal. Res.* **2008**, *32*, 361–376. [CrossRef]

14. Weil, J.A. EPR of iron centers in silicon dioxide. *Appl. Magn. Reson.* **1964**, *6*, 1–16. [CrossRef]

15. Sivaramaiah, G.; Lin, J.; Pan, Y. Electron paramagnetic resonance spectroscopy of Fe^{3+} ions in amethyst: Thermodynamic potentials and magnetic susceptibility. *Phys. Chem. Miner.* **2011**, *38*, 159–167. [CrossRef]

16. Weil, J.A. A review of electron spin resonance and its applications to the study of paramagnetic defects in crystalline quartz. *Phys. Chem. Miner.* **1984**, *10*, 149–165. [CrossRef]
17. Nilges, M.J.; Pan, Y.; Mashkovtsev, R. Radiation-damage-induced defects in quartz. I. Single-crystal W-band EPR study of hole centers in an electron-irradiated quartz. *Phys. Chem. Miner.* **2008**, *35*, 221–235. [CrossRef]
18. Pan, Y.; Nilges, M.J.; Mashkovtsev, R.I. Radiation-indiced defects in quartz. II. Single-crystal W-band EPR study of a natural citrine quartz. *Phys. Chem. Miner.* **2008**, *35*, 387–397. [CrossRef]
19. Mashkovtsev, R.I.; Pan, Y. Nature of paramagnetic defects in α-quartz: Progresses in the First Decade of the 21st Century. In *New Developments in Quartz Research: Varieties, Crystal Chemistry and Uses in Technology*; Novak, B., Marek, P., Eds.; Nova Science Publishers: Hauppauge, NY, USA, 2013; pp. 65–104.
20. Walsby, C.J.; Lees, N.S.; Claridge, R.F.C.; Weil, J.A. The magnetic properties of oxygen-hole aluminum centres in crystalline SiO_2. VI: A stable AlO_4/Li centre. *Can. J. Phys.* **2003**, *81*, 583–598. [CrossRef]
21. Botis, S.M.; Pan, Y. First-principles calculations on the $[AlO_4/M^+]^0$ (M = H, Li, Na, K) defects in quartz and crystal-chemical controls on the uptake of Al. *Mineral. Mag.* **2009**, *73*, 537–550. [CrossRef]
22. Anders, E.; Grevesse, N. Abundances of the elements: Meteoritic and solar. *Geochim. Cosmochim. Acta* **1989**, *53*, 197–214. [CrossRef]
23. Blankenburg, H.-J.; Götze, J.; Schulz, H. *Quarzrohstoffe*; Deutscher Verlag für Grundstoffindustrie: Leipzig-Stuttgart, Germany, 1994; p. 296.
24. Götze, J.; Plötze, M.; Graupner, T.; Hallbauer, D.K.; Bray, C. Trace element incorporation into quartz: A combined study by ICP-MS, electron spin resonance, cathodoluminescence, capillary ion analysis and gas chromatography. *Geochim. Cosmochim. Acta* **2004**, *68*, 3741–3759. [CrossRef]
25. Miyoshi, N.; Yamaguchi, Y.; Makino, K. Successive zoning of Al and H in hydrothermal vein quartz. *Am. Mineral.* **2005**, *90*, 310–315. [CrossRef]
26. Müller, A.; Koch-Müller, M. Hydrogen speciation and trace element contents of igneous, hydrothermal and metamorphic quartz from Norway. *Mineral. Mag.* **2009**, *73*, 569–583. [CrossRef]
27. Baron, M.A.; Stalder, R.; Konzett, J.; Hauzenberger, C.A. OH-point defects in quartz in B- and Li-bearing systems and their application to pegmatites. *Phys. Chem. Miner.* **2015**, *42*, 53–62. [CrossRef]
28. Frigo, C.; Stalder, R.; Hauzenberger, C.A. OH defects in quartz in granitic systems doped with spodumene, tourmaline and/or apatite: Experimental investigations at 5-20 kbar. *Phys. Chem. Miner.* **2016**, *43*, 717–723. [CrossRef]
29. Di Benedetto, F.; Innocenti, M.; Tesi, S.; Romanelli, M.; D'Acapito, F.; Fornaciai, G.; Montegrossi, G.; Pardi, L.A. A Fe K-edge XAS study of amethyst. *Phys. Chem. Miner.* **2010**, *37*, 283–289. [CrossRef]
30. Ramseyer, K.; Mullis, J. Factors influencing short-lived blue cathodoluminescence of alpha-quartz. *Am. Mineral.* **1990**, *75*, 791–800.
31. Götze, J.; Plötze, M.; Trautmann, T. Structure and luminescence characteristics of quartz from pegmatites. *Am. Mineral.* **2005**, *90*, 13–21. [CrossRef]
32. Perny, B.; Eberhardt, P.; Ramseyer, K.; Mullis, J.; Pankrath, R. Microdistribution of Al, Li, and Na in α-quartz: Possible causes and correlation with short-lived cathodoluminescence. *Am. Mineral.* **1992**, *77*, 534–544.
33. Götze, J.; Plötze, M.; Habermann, D. Cathodoluminescence (CL) of quartz: Origin, spectral characteristics and practical applications. *Mineral. Petrol.* **2001**, *71*, 225–250. [CrossRef]
34. Gorton, N.T.; Walker, G.; Burley, S.D. Experimental analysis of the composite blue CL emission in quartz. *J. Lumin.* **1996**, *72–74*, 669–671.
35. Van den Kerkhof, A.M.; Hein, U.F. Fluid inclusion petrography. *Lithos* **2001**, *55*, 27–47. [CrossRef]
36. Skuja, L. Optically active oxygen-deficiency-related centers in amorphous silicon dioxide. *J. Non-Cryst. Solids* **1998**, *239*, 16–48. [CrossRef]
37. Pacchioni, G.; Ierano, G. Optical absorption and nonradiative decay mechanism of E' centre in silica. *Phys. Rev. Lett.* **1998**, *81*, 377–380. [CrossRef]
38. Stevens-Kalceff, M.A.; Phillips, M.R. Cathodoluminescence microcharacterization of the defect structure of quartz. *Phys. Rev. B* **1995**, *52*, 3122–3134. [CrossRef]
39. Siegel, G.H.; Marrone, M.J. Photoluminescence in as-drawn and irradiated silica optical fibers: An assessment of the role of non-bridging oxygen defect centres. *J. Non-Cryst. Solids* **1981**, *45*, 235–247. [CrossRef]
40. Stevens-Kalceff, M.A. Cathodoluminescence microcharacterization of point defects in α-quartz. *Mineral. Mag.* **2009**, *73*, 585–606. [CrossRef]

41. Walderhaug, O.; Rykkje, J. Some Examples of the Effect of Crystallographic Orientation on the Cathodoluminescence Colors of Quartz. *J. Sediment. Res.* **2000**, *70*, 545–548. [CrossRef]
42. Sippel, R.F. Luminescence petrography of the Apollo 12 rocks and comperative features in terrestrial rocks and meteorites. In *Lunar and Planetary Science Conference Proceedings*; The M.I.T. Press: Cambridge, MA, USA; Volume 1, pp. 247–263.
43. Larsen, R.B.; Henderson, I.; Ihlen, P.M.; Jacamon, F. Distribution and petrogenetic behavior of trace elements in granitic quartz from South Norway. *Contrib. Mineral. Petrol.* **2004**, *147*, 615–628. [CrossRef]
44. Monecke, T.; Kempe, U.; Götze, J. Genetic significance of the trace element content in metamorphic and hydrothermal quartz: A reconnaissance study. *Earth Planet. Sci. Lett.* **2002**, *202*, 709–724. [CrossRef]